20

A New Approach to Analysis of Single-Molecule Force Measurements

Evan Evans, Ken Halvorsen, Koji Kinoshita, and Wesley P. Wong

Abstract A common aim in probing single molecular bonds or the structural stability of proteins is to measure the kinetic rates at which a bond dissociates or a protein changes conformation under conditions of changing force. Using sample data taken from tests of ligand–receptor unbinding and protein unfolding/refolding, we show that populations of "single molecule" events, arranged into statistical arrays expressing the numbers of bonds or initial conformers remaining as a function of time and cumulated into histograms of transitions over fixed time increments, provide the bases for a model-independent assay of the kinetic rates of transition throughout the course of an experiment. Most important, this assay for kinetic rates can be employed with any deterministic mode of force spectroscopy, whether the pulling force increases *or* decreases with time.

20.1. Introduction

In tests of molecular complexes or structures with force probes, the common objective is to measure the kinetic rate $k_{\rightarrow}$ at which a single complex (bond) dissociates or a single molecule changes conformation when subjected to a pulling force. As such, success in molecular force measurements requires an experimental approach that will produce a high probability of single-molecule events plus reliable criteria for excluding contaminating events that arise from irrelevant (nonspecific) and multiple molecule attachments. After briefly discussing ways to best satisfy these requirements, we show that arranging the refined population of putative "single-molecule" events into (1) an array $N(t_i)$ expressing the numbers of bonds or initial conformers remaining as a function of time and (2) its histogram $\Delta N_k(t_k)$ of transition events cumulated over fixed time increments Δt together establish a direct (model-independent) assay for the kinetic rates of transition, $k_{\rightarrow}(t_k) \approx (\Delta N_k/\Delta t)/N(t_k)$ defined at the mean sample times t_k. Although formulated here in terms of the ratios of probability density/probability for a two-state molecular transition [i.e., $p(t_k)/S(t_k) = k_{\rightarrow}(t_k)$],

E. Evans, K. Kinoshita • Department of Biomedical Engineering, Boston University, Boston, MA 02215, USA, and Physics and Pathology, University of British Columbia, Vancouver, BC Canada V6T 2A6
K. Halvorsen, W.P. Wong • The Rowland Institute at Harvard, Harvard University Cambridge MA 02142, USA

P. Hinterdorfer, A. van Oijen (eds.), *Handbook of Single-Molecule Biophysics*,
DOI 10.1007/978-0-387-76497-9_20,

the statistics-based approach can be readily extended to encompass more hierarchal and complex transitions if backed by appropriate evidence. Of fundamental significance, the experimental assay for kinetic rates provides a general method to analyze results obtained with any deterministic mode of force spectroscopy, $f(t)$, whether the pulling force increases *or* decreases with time. Using examples of ligand–receptor unbinding and protein unfolding/refolding, we demonstrate that plotting the experimental assay for kinetic rates on a logarithmic scale versus pulling force $f(t_k)$, and invoking Arrhenius phenomenology, $k_{\rightarrow}(f) = k_0 \exp[-\Delta G(f)/k_B T]$,[1] reveals both the impact of force on the chemical energy barrier governing the kinetics of single-molecule transitions, $\Delta G(f)/k_B T$, and the rate prefactor, $k_0 = 1/t_0$, characterizing persistence of the force-free state. As a preface to these examples, we first outline principles of instrument design and procedures for data processing that lead to reliable assays of molecular transitions—the obvious challenge being to acquire "single-molecule events".

20.2. Force Probe Design and the Quest for Single-Molecule Statistics

A molecular force probe is an ultrasensitive "spring" with a reactive tip that initiates the attachments to be tested. Thus, touched repeatedly to a target surface, the probe tip is prepared with a very low concentration of the initiator molecule to ensure rare discrete attachments. Since the reacting molecules on a tip and target surface are usually limited in range of mobility, the likelihood of forming attachments on touch depends primarily on the area of contact and to a much lesser extent on contact time. Consequently, the probe instrument should be designed to touch the target surface with a small (less than a few piconewtons) compressive force regulated by feedback. With both the impingement force and duration of touch controlled, the conditions leading to attachments will be nearly identical for every touch to a target, allowing the rare events to be viewed as a stationary-random process (amenable to characterization by Poisson statistics as described later). Equally important for the assay presented here, a probe must have sufficient precision to report forces with ~1-pN accuracy over a wide range from minus a few piconewtons to +100 pN or more. Thus, to achieve this accuracy, the probe transducer should have a low spring constant (less than or equal to a piconewton per nanometer), as well as a nanometer-precision system for tracking its tip displacement.

As an example, a biomembrane force probe (BFP) [1,2] was used to test the ligand–receptor bonds described later, providing the force–time traces seen in Figure 20.1. With a tunable spring constant set typically between $0.3 < \kappa_f < 0.5$ pN/nm and with 3- to 4-nm precision in video tracking of its tip, the BFP can measure forces in the range from –30 to +300 pN with a standard deviation (SD) of ±1–2 pN. As other examples, two types of laser optical trap force probes (OTFP) were used to test the unfolding/refolding of polyprotein domains [3,4]. With spring constants set typically between $0.005 < \kappa_f < 0.1$ pN/nm, the fast video tracking systems in these OTFP instruments, one with 2- to 3-nm precision [3] and the other with <1-nm precision [4,5], provide much better force accuracy, SD < ±0.1 pN, as demonstrated in Figure 20.2 (also later in Figure 20.9), than a BFP.

[1] Thermal energy $k_B T$ is ~4.08×10^{-21} J at room temperature.

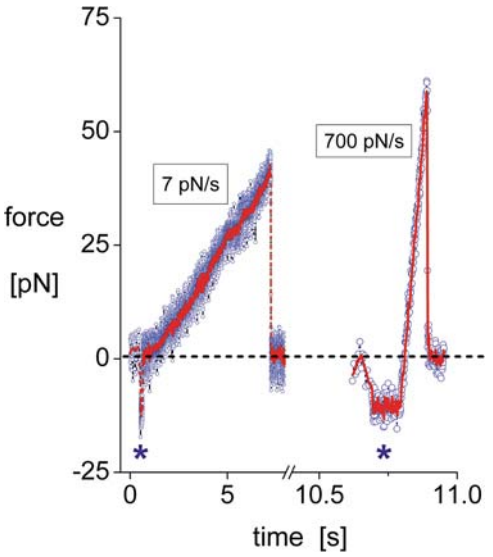

Figure 20.1. Force–time traces obtained from biomembrane force probe (BFP) in tests of ligand–receptor bonds: The left trace is at a slow (7 pN/s) ramp and the right trace is at a fast (700 pN/s) ramp of pulling force. A tenfold break in time axis separates the two traces to illustrate the major reduction in bond lifetime (i.e., from ~7 sec to ~0.1 sec) that accompanies the increase in its mechanical strength (i.e., from ~40 pN to ~60 pN) when ramps increase from slow to fast rates. Stars mark feedback control of the soft impingement (~–10 pN) and a brief, 0.1-sec period of contact ending with piezo retractions of the microsphere targets at fixed speeds. The red traces are five-point moving averages of the direct traces (blue) obtained at a sampling rate of 1,500/sec. Limited by uncertainty (~±4 nm standard deviation [SD]) in video tracking of the BFP tip deflection, the spread in force (~± 2-pN SD; *blue traces*) increases and decreases, in proportion to the spring constant k_f chosen for the experiments (here set to 0.5 pN/nm by micropipet suction).

However, smaller ranges of force are usually accessible to optical trap instruments, for example, –10 to +50 pN. Since rates of molecular transitions increase rapidly when subjected to increasing force, probe instruments have to provide high levels of precision at very fast sampling frequencies, which are limited to ~2–3 × 10^3/sec by viscous damping for the BFP and OTFP.

In most of the experimental examples described here, molecules were stressed by retracting a tip or target away from contact at fixed speed v_{pull}, resulting in a "force ramp." Although programmed to achieve a ramp of $\kappa_f v_{\text{pull}}$, the actual ramp produced by steady speed retraction depends on the effective stiffness κ_{eff} of the probe spring in series with the tip–target interfacial structure. For tests exhibiting linear force increases with time (cf. Figures 20.1 and 20.2), the tip–target interfaces respond like elastic springs, $\kappa_{t\sim t}$, and therefore, $\kappa_{\text{eff}} = \kappa_f \kappa_{t\sim t}/(\kappa_f + \kappa_{t\sim t})$. Thus, the ratio of observed ramp/nominal ramp, $c_{\text{rf}} = r_f/(\kappa_f v_{\text{pull}})$, provides a direct assay of the tip–target interfacial stiffness, $\kappa_{t\sim t} = \kappa_f\, c_{\text{rf}}/(1 - c_{\text{rf}})$. As an example, using amino- or mercapto-silane and hetero-bifunctional polymer linkers to immobilize proteins on glass microspheres, one finds the ratios c_{rf} to depend on the molecules chosen, typically exhibiting values between 0.7 and 0.9 with small SD (<±0.1). Close to 1, this range of values shows that the tip–target interface is much stiffer than the probe spring.

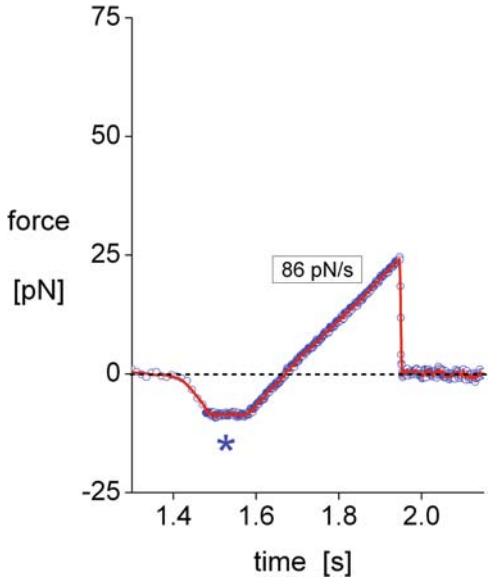

Figure 20.2. Force–time trace from a laser OTFP test. Replacing a biomembrane force probe (BFP) as the transducer in a nearly identical apparatus, the probe is a microsphere confined by a focused laser beam [3]. Controlled by feedback and moved by a piezo as in Figure 20.1, a target microsphere was driven to contact the probe with ∼–8-pN impingement (*star*) for 0.1 sec, then retracted at a fixed speed to stress an attachment with a ramp of 90 pN/sec until rupture. The red trace is a five-point moving average of the direct trace (*blue*) obtained at a sampling rate of 1,500/sec. Limited by the uncertainty (∼± 2-nm standard deviation [SD]) in video tracking of the probe deflection, the narrow spread in force (∼±0.1-pN SD, *blue trace*) demonstrates the better precision obtained with the softer OTFP spring constant (here, $k_f \sim 0.05$ pN/nm) set through control of the laser intensity.

20.3. Identifying Events Arising from Nonspecific and Multiple-Specific Attachments

Even using the type of probe instrument just described and controlling contact conditions, we still need to define procedures for dealing with the contaminating events that arise from nonspecific interactions and multiple-molecule attachments. Used to great advantage in testing unfolding/refolding of polyprotein domains with atomic force microscopy (AFM), one approach has been to accept only force–time traces showing "sawtooth" patterns with force increases and sharp drops equal to or less than the number of domains present in a single protein chain. Similarly, in testing weak molecular bonds, force traces with obvious multiple force drops are rejected. Yet, this method of inspection will not identify nonspecific attachments. Moreover, because of limits in time resolution, probe response, and fluctuations in force, a significant fraction of multiple attachments seem to escape detection[2] when compared to predictions from Poisson statistics (described later). Consequently,

[2] Subjected to large forces, preemptive failure of one component in a cluster of attachments will immediately transfer the load to the remaining components, resulting in an extremely rapid sequence of failures with little separation in time [6]. Because of probe response and fluctuations, only the final outcome of this sequence of events—a single drop to zero force—is likely be detected in most force–time traces. The only evidence of the multiple bonds is the large magnitude of breaking force reported by the probe.

we will demonstrate a simple conservative procedure to identify the major subset of "raw statistics" that most likely contains the "single-molecule" events. After describing the procedures, we will illustrate their impact on "raw statistics" with data from tests of molecular unbinding.

20.3.1. Dealing with Nonspecific Events

Performed under the same conditions of target impingement and retraction speed as in the tests of functional properties, we employ control experiments to identify which bins in histograms are likely to contain significant numbers of nonspecific events. Since nonspecific interactions in controls arise mainly at low forces, the simplest approach is to ignore this low range of forces in histograms when the numbers become significant. Although the approach is unsophisticated, we will show that ignoring these short-time statistics has no effect on the assay for transition rates at longer times and higher forces. The procedure merely sets a lower bound to the range of data analyzed. Most of the studies to be described here involve molecules immobilized on rigid surfaces at concentrations adjusted to yield <15%–20% specific attachments from thousands of repeated contacts. With these preparations, control experiments typically yield tenfold fewer attachments. As a demonstration relevant to later examples, Figure 20.3 shows force histograms obtained from tests in NaCl buffer plus 5 mM ethylenediaminetetraacetic acid (EDTA) between a microsphere tip linked covalently with intercellular adhesion molecule-1 (ICAM-1) and a microsphere target presenting recombinant β_2-integrin lymphocyte function-associated antigen-1 (LFA-1) held by a covalently linked activating antibody (240Q [7,8]). Touched ~1,400–1,800 times at a force of –10 pN (for 0.1 sec), less than 1%–2% of the tip–target contacts in EDTA indicated an attachment.

In marked contrast to microsphere targets, even when performed with the same soft touch and brief contact, controls for interactions at surfaces of biological cells yield much higher frequencies of nonspecific attachments and larger ranges of forces affecting statistics. Strongly dependent on the speed of target retraction, the increased number of nonspecific attachments and range of forces are primarily consequences of a much larger area of contact at a cell surface and the stronger hydrodynamic coupling ("suction") that accompanies fast retraction of the "soft" target [2]. Demonstrating the enhanced nonspecific interaction with cell surfaces, Figure 20.4 shows another set of controls relevant to LFA-1 interactions in which a probe linked with an irrelevant protein (bovine serum albumin) was touched against human neutrophilic leukocytes (PMNs), this time in buffer plus 2 mM Mn^{2+}. Although large numbers of nonspecific forces are seen at fast retraction speeds in Figure 20.4, well-defined populations of specific-integrin attachments can be observed beyond the range contaminated by nonspecific events when a probe decorated with low concentration of ICAM-1 is touched to PMNs in Mn^{2+}. As we show in a later example (Figure 20.8), simply ignoring this initial force range leaves the prominent peak of specific events amenable to analysis.

20.3.2. Dealing with Multiple-Specific Events

Unlike nonspecific interactions, the procedure for identifying and excluding hidden events that originate from multiple attachments is not benign and must be considered carefully. Since definitive observational criteria are usually not available for rejecting events,

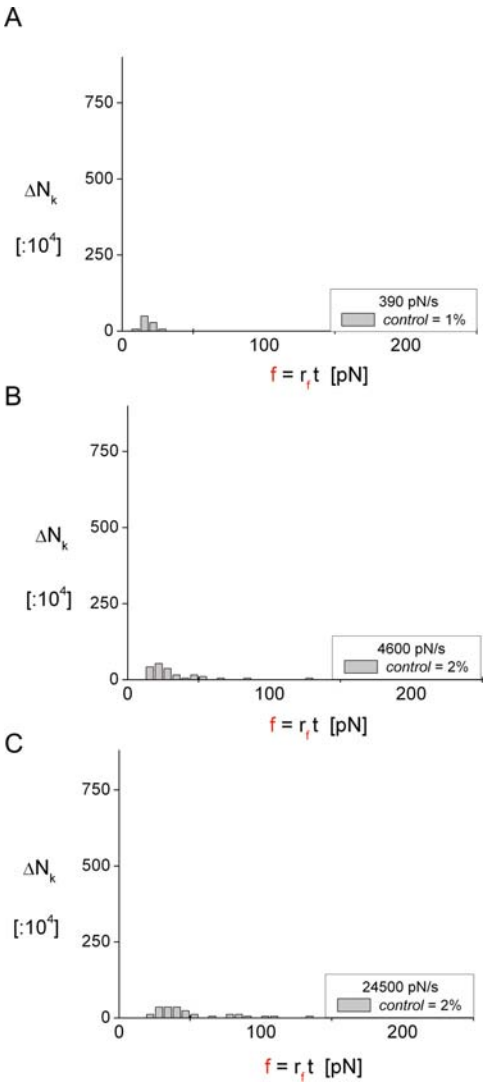

Figure 20.3. Controls for nonspecific interactions in tests of lymphocyte function-associated antigen-1 interactions that involve immobilized constructs on glass microspheres. Performed at three force rates in NaCl buffer plus 5 mM ethylenediaminetetraacetic acid, force histograms show the numbers of nonspecific attachments (scaled per 10^4 touches) obtained from 1,400–1,800 touches between a biomembrane force probe tip linked covalently with intercellular adhesion molecule-1 and the microsphere targets presenting recombinant $\alpha_L\beta_2$ integrin held by a covalently linked activating antibody (240Q [6]).

the primary objective in all experiments should be to establish a stationary-random process for formation of attachments, employing sensitive feedback to control the initial contact and reducing the concentration of molecular reactants to achieve *rare* events. Once accomplished, the attachment frequency A_ω can be used to define the probability $P_0 = (1 - A_\omega)$ for no attachment, from which Poisson estimates follow for the probabilities of a single attachment,

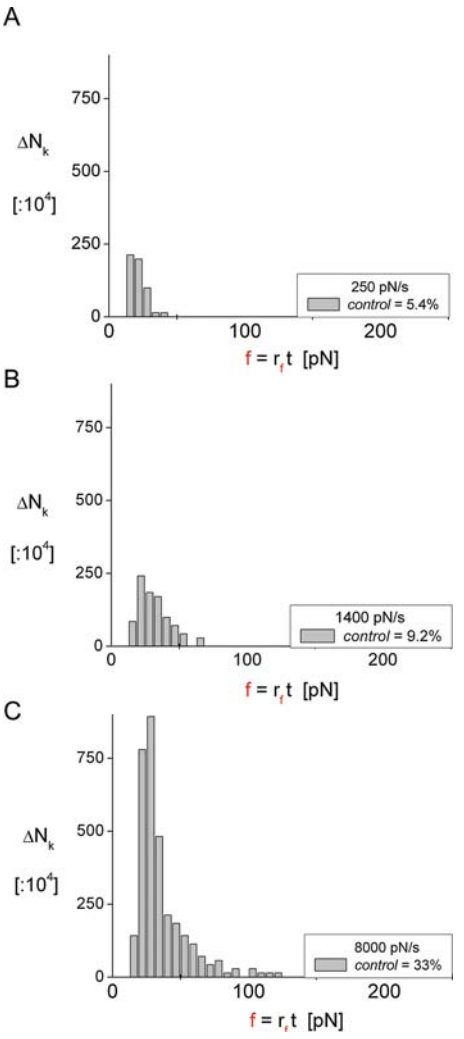

Figure 20.4. Controls for nonspecific interactions in tests of lymphocyte function-associated antigen-1 (LFA-1) interactions at the surfaces of human neutrophilic leukocytes (PMNs). Performed at three force rates in buffer plus 2 mM Mn^{2+}, force histograms show the numbers of nonspecific attachments (scaled per 10^4 touches) obtained from ~1,000 touches between a biomembrane force probe tip linked covalently with an irrelevant protein (bovine serum albumin) and PMNs expressing LFA-1.

$P_1 = (A_\omega - 1)\ln(1 - A_\omega)$, and all multiples, $P_{n\geq 2} = A_\omega + (1 - A_\omega)\ln(1 - A_\omega)$. Since multiple attachments share the applied force (albeit with unknown distribution), we expect their transitions (detachments or conformational changes) to occur at unusually long times and very large forces.Hence, we use the probability for multiples to conservatively identify a small fraction of events $P_{n\geq 2}/A_\omega$ (typically ~10%–15% or less) to be excluded at the longest transition times (largest forces). Although there are only a few events, we show next that truncating "raw statistics" by this precise fraction produces arrays of events $N(t_i)$ with appropriate convergence at long times.

20.4. Establishing Estimators for Initial State Probability and Distribution of Transitions

Using data from tests between a BFP linked with ICAM-1 and microsphere targets linked with recombinant LFA-1 ($\alpha_L\beta_2$-LZ [9]), we will first demonstrate how to obtain estimators for initial state probability and its probability distribution of transitions.[3] As noted in the introduction, these two observables form the basis for the direct assay of the kinetic rates in force probe experiments. Figures 20.5A, B show examples of the arrays $N(t_i)$ (open blue circles) defining unnormalized probabilities of bond survival, which were obtained by excluding a small number of "Poisson multiples" at the terminus (long-time tail) of each "raw data" set (open black circles). Equivalent to time (i.e., $f = r_f t$), the numbers of integrin attachments $N(t_i)$ that survived in 2 mM Ca^{2+} are plotted as a function of force in Figure 20.5A for a ramp of 770 pN/sec. Based on 417 attachments from 1,703 cycles of approach-touch-retraction, the Poisson fraction $P_{n\geq 2}/A_\omega \approx 0.134$ marked 56 events for exclusion from the "raw data" tail. Similarly, the numbers of integrin attachments that survived in 2 mM Mg^{2+} are plotted in Figure 20.5B as a function of force for a ramp of 89 pN/sec. In total, 375 attachments were detected from 1,804 cycles of approach-touch-retraction. Again from the attachment frequency, the Poisson fraction $P_{n\geq 2}/A_\omega \approx 0.112$ marked 42 events for exclusion from the "raw data" tail. Establishing unnormalized estimators for initial state probabilities $[S_1(t_i)]$, the arrays $N(t_i)$ (open blue circles) in Figures 20.5A, B are expected to be enriched significantly in "single-molecule" events, which is consistent with the rapid convergence in statistics observed at large forces (long times). Plotted directly below in Figures 20.5C, D, histograms of the "raw data" show the bins of events that were excluded at long times (cross-hatched), as well as the few nonspecific events expected from controls (gray bins) at low forces. As described later, the intervening (bright yellow) bins represent the numbers ΔN_k of unbinding transitions within fixed sampling periods Δf ($= r_f\ \Delta$t), providing the estimators for probability density p(t_k) and the rate of decrease in the initial state probability, $p(t_k) = -[dS_1/dt]_k$. Unless supported by additional evidence, more-aggressive truncations of the raw data to obtain these estimators would be unsubstantiated and likely to introduce artifacts in the assay of kinetic rates.

20.5. Two-State Transitions and the Direct Experimental Assay for Kinetic Rates

Applicable to many types of single-molecule tests, the estimators for initial state probability, i.e., $S_1(t) \approx N(t_i)/N(0)$, characterize the likelihood that single-molecular complexes or conformers remain in the initial state throughout the course of an experiment. Treated here as a two-state transition, a first-order Markov equation describes the temporal evolution of this initial state to a subsequent state $S_2(t)$ of molecular dissociation or new conformation, that is,

$$dS_1(t)/dt = -k_{\rightarrow}(t)S_1(t) + k_{\leftarrow}(t)[1 - S_1(t)]$$

$$S_2(t) \equiv [1 - S_1(t)]$$

[3] Used in this chapter to illustrate the analysis of force distributions in ligand–receptor dissociation under force ramps, the sample data for interactions between ICAM-1 and β_2-integrin (LFA-1 on leukocytes and recombinant $\alpha_L\beta_2$-LZ heterodimer) are taken from a two manuscripts describing many tests of LFA-1 integrin interactions, which have been submitted to the *Biophysical Journal* for publication.

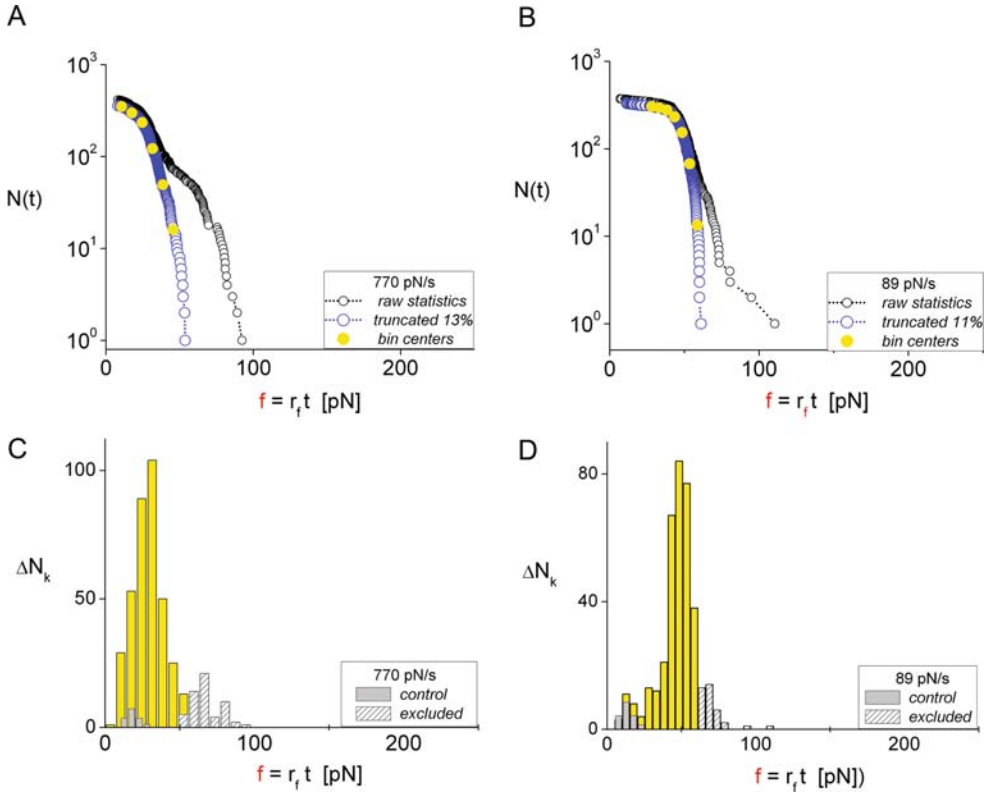

Figure 20.5. Unbinding intercellular adhesion molecule-1 attachments to $\alpha_L\beta_2$ immobilized on microspheres with ramps of force. **A.** Tests in 2 mM Ca^{2+} at a ramp rate of 770 pN/sec produced 417 attachments from 1,703 contacts. Thus, a Poisson fraction of 56 putative multiples was marked for exclusion from the "raw statistics" (*black open circles*), yielding the unnormalized estimator $N(f_k)$ for initial-state probability (*blue open circles*). **B.** Tests in 2 mM Mg^{2+} at a ramp rate of 89 pN/sec produced 375 attachments from 1,804 contacts. Thus, a Poisson fraction of 42 putative multiples was marked for exclusion from the "raw statistics," again yielding the unnormalized estimator $N(f_k)$ for initial-state probability. **C, D.** Histograms of the "raw data" appearing in panels A and B. The cross-hatched bins identify the events truncated from the "raw statistics" at long times to obtain the unnormalized estimator for initial state probability $N(t_i)$. The gray bins represent the nonspecific events expected from controls scaled to match the appropriate number of contacts. The bright-yellow bins containing the majority of events represent the numbers ΔN_k of transitions occurring within fixed sampling periods $\Delta f\,(= r_f\,\Delta t)$, yielding the unnormalized estimators for probability density, $p(t_k) = (r_f/\Delta f)\Delta N_k$, at the bin centers $f_k = r_f t_k$. (The closed yellow circles in panels A and B identify interpolation points.)

Governing the two-state dynamics are the instantaneous frequencies of forward $k_{\rightarrow}(t)$ and reverse $k_{\leftarrow}(t)$ transitions. Since application of pulling forces with a "soft" spring eliminates reverse transitions [10,11], we approximate $k_{\leftarrow}$ as $\sim$0 and reduce the two-state dynamics to a first-order decay process, $dS_1(t)/\mathrm{dt} \approx -k_{\rightarrow}(t)S_1(t)$, the solution of which reflects the cumulated frequency of forward transition, that is, $S_1(t) = \exp[-\int_{0\rightarrow t} k_{\rightarrow}(t')\,dt']$. As such, the probability density $p(t)$ now represents the "instantaneous" rate, $k_{\rightarrow}(t)S_1(t)$, at which forward transitions drain the initial state, and the ratio of probability density/probability becomes equivalent to the forward kinetic rate, $k_{\rightarrow}(t)$, at any time. Hence, equally important in our approach to data analysis, the numbers of events ΔN_k in histograms, cumulated over discrete

time differences Δt, provide key estimators for probability density, $p(t_k) \approx (1/\Delta t)[\Delta N_k/N(0)]$, at the bin center times t_k. Interpolating among the array $N(t_i)$ to obtain the values $N(t_k)$ (identified by solid yellow circles in Figures 20.5A–B), we establish the ingredients needed to specify ratios $p(t_k)/S(t_k)$ of probability density/probability and to directly assay the forward kinetic rates, $k_{\rightarrow}(t_k)$. Perhaps most significant, this generic assay for kinetic rates is valid even when transition rates vary over time, which allows the approach to be applied in all modes of force spectroscopy as long as the history of force follows a precise function in time $f(t)$. Since the estimator for probability density/probability, $(1/\Delta t)\ [\Delta N_k/N(t_k)]$, is independent of $N(0)$, the results do not depend on the initial force (i.e., time) where we commence the analysis, which allows us to simply ignore bins at low forces in histograms containing large numbers of nonspecific events.

In the sections that follow, we will demonstrate this method of analysis using data from a variety of experiments. Along with the requirement for a well-defined population of single-molecule transitions, the key assumption underlying validity of the two-state approach is that the internal dynamics of transitions (e.g., pausing at metastable states or involving multiple reaction pathways) must be orders of magnitude faster than the mean time needed to reach the end state. Even so, prominent consequences of internal transitions can be perceived through exploring a large range of force or force ramps, as recognized some time ago [12].

20.6. Experimental Example: Dissociating ICAM-1 from β_2-Integrin with Force Ramps

20.6.1. Microsphere Targets

In analyzing data from force ramp experiments, we employ an equivalent and very useful transformation that replaces the statistical estimators based on transition times with those based on forces, that is, $p(t_k)/S(t_k) \equiv r_f\, p(f_k)/S(f_k)$.[4] By changing from transition times t_k to force statistics $f_k = r_f t_k$, we will determine the ratios of probability density/probability, $p(t_k)/S(t_k) \approx (r_f\,/\Delta f)[\Delta N_k/N(f_k)]$, from the bin contents in force histograms ΔN_k and values for $N(f_k)$ obtained at the bin centers f_k by interpolation among the initial state statistics $N(f_i)$. Finding these ratios from data at several ramps like the examples shown in Figure 20.5, we plot the results on a logarithmic scale in Fig. 20.6A, B to expose the dramatic increases in off-rates that accompany increases in the forces. Moreover, starting from their intercepts at zero force, the off-rates of ICAM-1 from LFA-1 are seen to differ significantly in the two divalent cation environments. Extended to higher and lower forces with ratios from faster and slower ramps (solid green, magenta, red circles in Fig. 20.6A, B), the marked difference in kinetics becomes clear when comparing the linear regressions superposed on each data set. Converted to a linear scale, the fits yield exponentials: $k_{\rm off} \approx (2/\text{sec})\ \exp(f\,/9.6\ \text{pN})$ for activation in Ca^{2+} and $k_{\rm off} \approx (0.007/\text{sec})\ \exp(f\,/6.8\ \text{pN})$ for activation in Mg^{2+}. Differing more than 100-fold, the force-free dissociation rates obtained from the single-molecule assay are found to be consistent with results ($k_0 \sim 1$/sec in Ca^{2+} and ~ 0.01/sec in Mg^{2+}) known from previous solution-based assays [13].

[4] Note, after we submitted this chapter, a similar version of the approach described here based on analysis of force histograms was published independently by Dudko, Hummer, and Szabo (in *Proc. Natl. Acad. Sci.*105: 15755–15760, 2008). Included in their paper are excellent applications to data from tests of nanopore unzipping of DNA hairpins and tests of unfolding a protein attached by flexible linkers to an atomic force microscope.

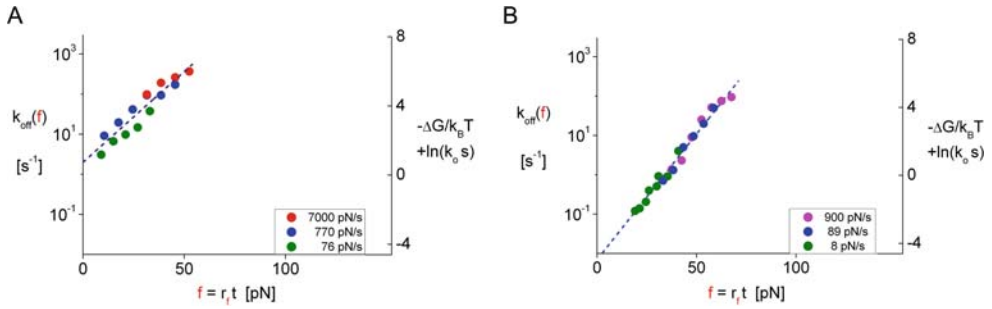

Figure 20.6. Rates of unbinding of intercellular adhesion molecule-1 (ICAM-1) attachments to $\alpha_L\beta_2$ immobilized on microspheres under slow to fast ramps of force. (Examples of the experimental estimators defining these ratios are shown in Figure 20.5 for one ramp rate.) Plotted on logarithmic scales versus unbinding force, the ratios of probability density/probability defining off rates **(A)** for tests in 2 mM Ca^{2+} at 76 and 770 pN/sec (plus those up to 55 pN at 7,000 pN/s) and **(B)** for tests in 2 mM Mg^{2+} at 7, 90, and 740 pN/sec. The regression lines superposed on the data reveal that the off-rates of single-molecular complexes in both cation environments increase exponentially over these ranges of pulling force (expressions for the off-rate dependences appear in the text). Scales at the right quantify the shifts in activation energy of ICAM-1 bonds to $\alpha_L\beta_2$ produced by force, decreasing by nearly 8 units of thermal energy (~20 kJ/M) relative to the force-free state.

Viewed in the context of Arrhenius phenomenology, that is, $\ln[k_{off}(f)] - \ln(k_0) = -\Delta G(f)/k_BT$, the single-molecule force assays in Figures 20.6A, B reveal that large reductions in the activation energies account for the enormous increases in off-rates (note the scales added at the right). The thermal force f_β for lowering an activation energy by one k_BT characterizes the length gained in a molecular transition[10,11], which, based on the regressions in Figures 20.6A, B, are ~0.4 and 0.6 nm, respectively. At the same time, the correlations to off-rates (like those plotted in Figures 20.6A, B) provide a direct check on the quality and self-consistency of each assay. Converted to analytical expressions for forward transition rates $k_{\rightarrow}(f)$, the correlations predict initial state probabilities, $S_1(f) = \exp[-(1/r_f) \int_{0\rightarrow f} k_{off}(f')\, df']$, that can be compared directly to the statistics from all experiments.

Even when one is matching data from tests over a large span in ramps, a subsequent prominent deviation from the expected initial state probability at faster ramps can reveal a significant change in the energy landscape or pathways governing the kinetic rate. This outcome is demonstrated in Figures 20.7A, B with results for the LFA-1 interactions obtained at very fast ramps, 7,000 pN/s in Ca^{2+} and 8,400 pN/s in Mg^{2+}, respectively. Coinciding with the departures of the experimental statistics $N(t)$ (open blue circles) from the statistics $N_0S_1(t)$ (black dashed curves) predicted by off-rates at ramps <1,000 pN/s, broad wings of forces in distributions are found to extend beyond >55 pN in tests at 7,000 pN/s with Ca^{2+} and beyond >75 pN in tests at 8,400 pN/s with Mg^{2+} (bin locations marked by red-rimmed white circles in Figures 20.7A, B). Including measurements of forces and times at the very fast ramps, we see in Figures 20.7C, D that a new branch of off-rates (open red circles) has emerged from the results at ramps <1,000 pN/sec. The off-rates now increase little with increase in force, suggesting a significant alteration in the kinetic pathway for dissociation. [Note that, as demonstrated by the sharp drops in $N(t)$ beyond the last bin analyzed (last red-rimmed white circle), the largest forces arising from the emergent pathway ultimately became obscured by the Poisson fraction of putative multiples marked for exclusion. Hence, to obtain an accurate picture of any emergent pathway, it is essential to have a reliable (and conservative) procedure for truncating the "raw statistics".]

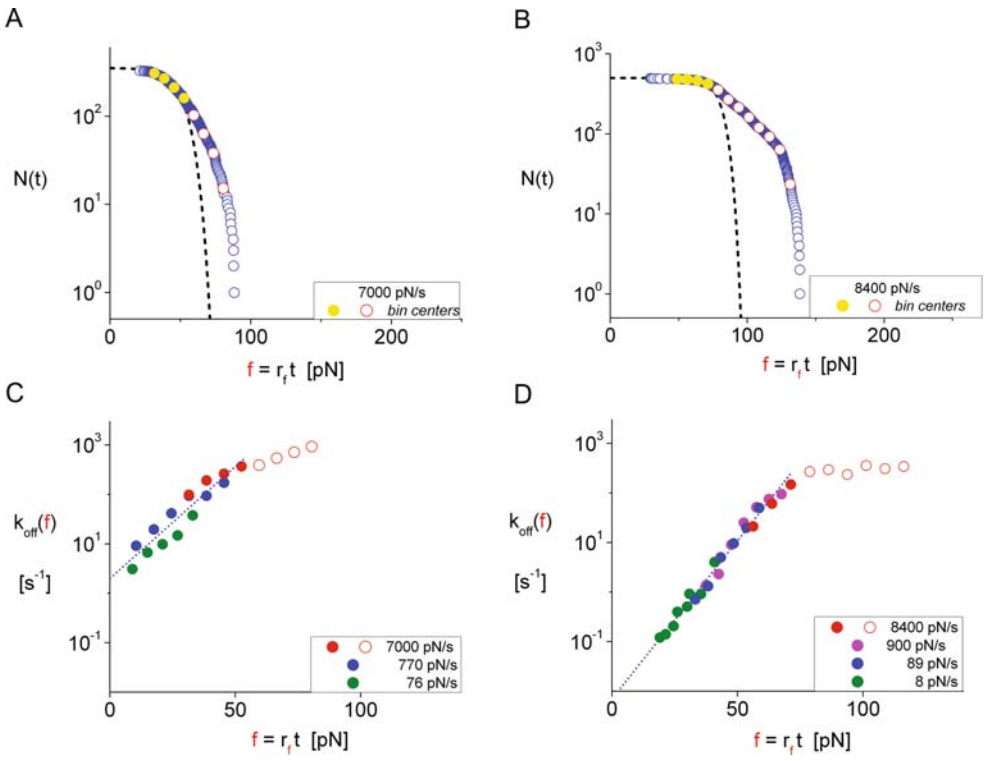

Figure 20.7. Rates of unbinding of intercellular adhesion molecule-1 attachments to $\alpha_L\beta_2$ immobilized on microspheres under extremely fast ramps of force. Plotted on a log scale versus force, experimental statistics for bond survival (*open blue circles*) for **(A)** tests in Ca^{2+} at 7,000 pN/sec and **(B)** for tests in Mg^{2+} at 8,400 pN/sec, both sets of data showing marked deviations from the statistics $N_0S_1(t)$ (*black dashed curves*) predicted by off-rate correlations at ramps <1,000 pN/sec. Coinciding with these deviations and identified by red-rimmed white circles for the bin centers, histograms of the data yield broad distributions of forces that extend well beyond the ranges expected from results in Figures 20.6A, B. By incorporating statistics from tests at these very fast ramps, the added ratios of probability density/probability (*red open circles*) are seen **(C, D)** to branch abruptly from the correlations at ramps <1,000 pN/sec, suggesting a significantly altered or reconfigured kinetic pathway for dissociation.

20.6.2. PMN Targets

For comparison to the experiments with recombinant β_2-integrin immobilized on microspheres, the following example demonstrates application of the approach to tests of LFA-1 interactions at the surfaces of human neutrophilic leukocytes (PMNs). Designed to quantify the impact on off-rates of a phenomenon called "inside-out" signaling in cells, the data presented in Figure 20.8 were taken from tests of an ICAM-1 probe against PMN surfaces following suspension in a buffer containing 2 mM Mg^{2+} plus soluble IL-8 (recombinant human chemokine, interleukin-8). With attachment frequency decreasing monotonically following exposure to IL-8, experiments had to be performed as quickly as possible (typically within a window of 5–10 min) after chamber preparation. By doing this, sufficient numbers of events were collected to clearly define narrow peaks like that seen in Figure 20.8A.

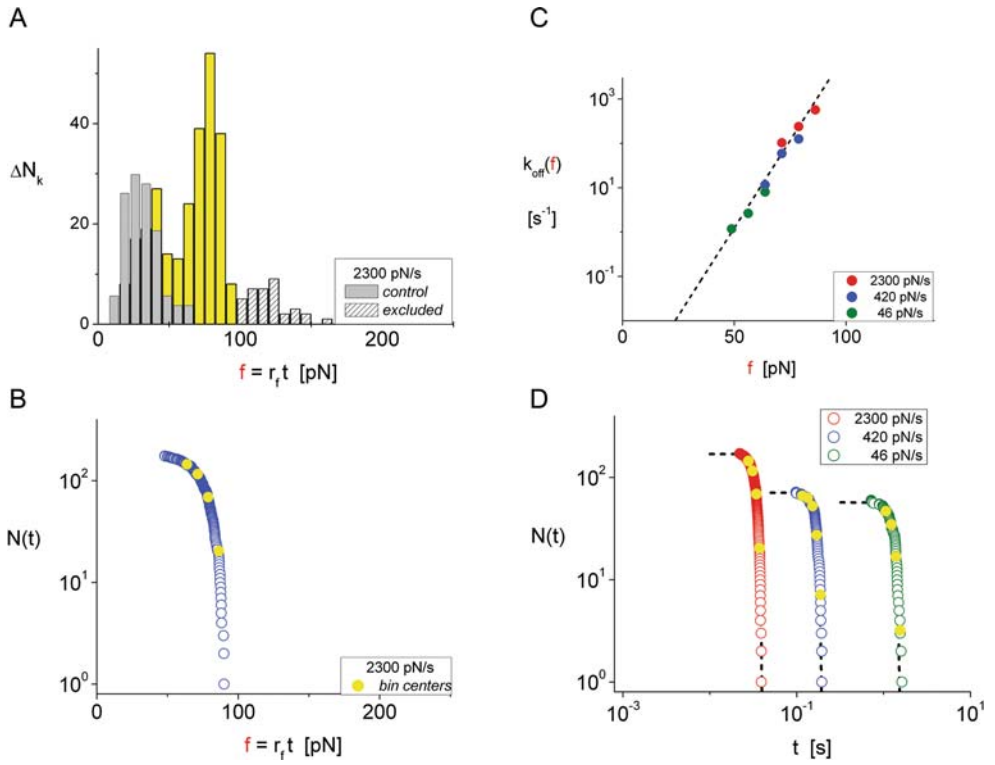

Figure 20.8. Rates of unbinding intercellular adhesion molecule-1 (ICAM-1) attachments to lymphocyte free antigen-1 (LFA-1) expressed on neutrophilic leukocytes (PMNs) under force ramps when stimulated by the chemokine interleukin-8 (IL-8). **A.** Obtained in 10 nM IL-8 plus Mg^{2+}, the histogram of "raw data" at 2,300 pN/sec illustrates the experimental estimator for probability density. **B.** Plotted directly below (on a log scale versus force are the corresponding statistics that characterize probability of bond survival (*open blue circles*). **C.** With ratios of probability density/probability from tests at three ramps in IL-8 plus Mg^{2+}, the off-rates reveal that unbinding of ICAM-1 from LFA-1 on PMNs stimulated by chemokines is dramatically slower than unbinding from LFA-1 on microspheres in Mg^{2+}. **D.** Providing a critical check on the assay for off-rates, the experimental statistics obtained at all the ramps are compared on a log-log scale versus time to the unnormalized probabilities $N_0 S_1(t)$ (*black dashed curves*) predicted by the off-rate correlation in panel C, i.e., $k_{\text{off}}(f) \approx (0.0001/\text{sec}) \exp(f/5.5\ \text{pN})$.

Narrow peaks in force ramp distributions reveal precipitous shortening in the lifetime of the bonds under the rising force, which appears as very rapid attenuation in long-time tails of the arrays $N(t)$ as shown in Figure 20.8B. Again with the ratios of probability density/probability provided by these experimental estimators, we plot the values on a logarithmic scale in Figure 20.8C to assay the off-rates of ICAM-1 from LFA-1 on chemokine-stimulated PMNs in Mg^{2+}. When compared to the results in Figure 20.6B for LFA-1 on microspheres in Mg^{2+}, the outcome demonstrates that chemokine stimulation and the "inside-out" signaling process dramatically increase the lifetime and strength of a single LFA-1 interaction. Again as a check on quality of the assay, the experimental statistics for different ramps are compared on a log-log scale versus time in Figure 20.8D to the unnormalized probabilities $N_0 S_1(t)$ (black dashed curves) predicted by the correlation in Figure 20.8C.

20.7. Experimental Example: Unfolding/Refolding of a Polyprotein with Force Ramps

Demonstrating the diversity of this approach, our final examples illustrate applications to unfolding and refolding of polyproteins. Created by Jane Clark at Cambridge University [14], the polyprotein in this example was an eight-mer sequence of four heterodimers: the R16 triple-helical repeat from chicken brain spectrin, followed by an I27 domain from cardiac muscle titin. Pulling on these polyproteins with an AFM, the creators showed that the spectrin triple-helical repeats unfold at forces between ∼30 and 50 pN under pulling speeds in a range from ∼1–4 × 10^3 nm/sec [14]. Yet, as expected from earlier studies (see references in Ref. 15), the I27 domains remain tightly folded until several-times larger forces are reached (∼150–180 pN). Less well established in probe tests of weak domains like R16, the objective here is to demonstrate a direct assay for rates of unfolding and refolding polyproteins using the experimental statistics and histograms of transitions obtained under ascending and descending ramps of force, respectively.

To achieve the precision in force and time needed to quantify these kinetic rates, the poly-R16/I27 construct was tested with two arrangements of a laser OTFP, one providing data at frequencies of 1,500/sec for fast-pulling experiments (see Figure 20.2 and Ref. 3) and the other providing data at slower frequencies of ∼200/sec but with subnanometer precision in chain length displacements (see Figure 20.9 and Refs. 4 and 5). Tethered to glass targets through linkages to a cysteine residue at the C-terminus, the polyprotein attachments in tests were obtained by capturing the polyhistidine residues at the N-terminus with an anti-His–linked OTFP microsphere. Illustrating the kinematics of unfolding and refolding four R16 domains, Figure 20.9 shows the changes in length (upper panel) of a single poly-R16/I27 protein produced by the cycle of positive–zero–negative force ramps seen in the lower panel.

20.7.1. Unfolding Kinetics

Examining unfolding first, we focus on forces obtained from traces showing one or more unfolding events at two ramp rates (10 and 473 pN/sec). Unfortunately, when tested at the fast ramp, preemptive failure of the noncovalent linkages left just over half of the traces showing only one unfolding event, with the next significant population showing two unfolding events; taken together, the two types of traces accounted for nearly 90% of the results. Based on statistics of the first unfolding events at 473 pN/sec, Figures 20.10A, B demonstrate the force histogram and the experimental statistics characterizing the fastest unfolding kinetics in the OTFP experiments. For more slowly unfolding kinetics, we use the forces for two unfolding events from experiments performed with the high-resolution instrument at the slow ramp 10 pN/sec, where most traces contained more than two unfolding events. Under slow loading, longer times are needed to unfold domains and the events occur at lower forces. Finding ratios of probability density/probability from both sets of data, we plot two assays for unfolding rates on a logarithmic scale versus force in Figure 20.10C. As shown by gray dashed lines in Figure 20.10C, both assays correlate well with a common exponential dependence on force [i.e., ∼exp(f/2.8 pN)], separated by approximately twofold difference in the preexponential factors describing "spontaneous" unfolding rates. This shift is qualitatively consistent with the different numbers of unfolding events treated in the two cases. However, not knowing the total number of folded domains in the attachments prior to test, we can only estimate the frequency for unfolding a single spectrin R-16 domain. Thus, assuming that four folded and

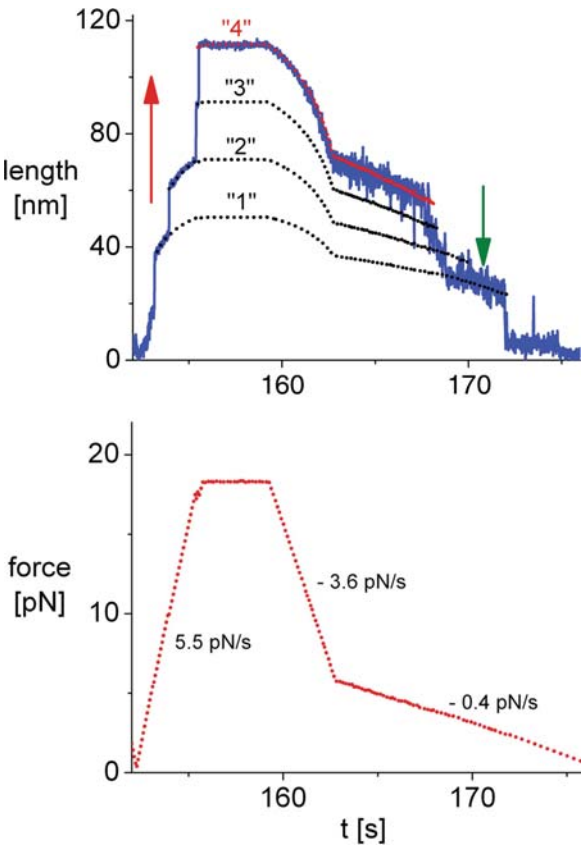

Figure 20.9. Changes of length (*blue traces, upper panel*) produced in a single poly-R16/I27 protein by a sequence of positive– zero–negative force ramps (*red traces, lower panel*). Performing repeated cycles of pulling and relaxing attached chains parallel to the optical axis of an inverted microscope, the OTFP apparatus employed reflection interference contrast optics and unique image analysis software to measure displacements of the probe microsphere with subnanometer precision [4,5]. Centered well above the coverglass floor of a microchamber, the strength of the trapping potential was varied by controlling the laser intensity. Because of the large distance to the trap center and the soft confinement along the optical axis, the force history applied to the microsphere was unaffected by the increases and decreases in length of the polyprotein, appearing only as extremely small blips in the red force trace. Correlated to the length increases in unfolding (*upward red arrow*) and decreases in refolding (*downward green arrow*), separations between the black dashed curves are predicted by adding a length $L_c \sim 37$ nm at each step to the thermally fluctuating contour length described by a "worm-like chain" with persistence length $b \sim 0.7$ nm while, at the same time, substracting 5 nm to account for the folded domain.

noninteracting domains were present in each attachment, the correlation for first unfolding events in the fast ramp test (red closed circles, Figure 20.10D) implies an unfolding rate of 0.009/sec $\div$ 4 $\approx$ 0.0023/sec for a single domain, which is close to results from solution-based assays [16]. Again checking the quality and self -consistency of the assays, experimental statistics from both tests are compared on a log-log scale versus time in Figure 20.10D to the unnormalized probabilities $N_0 S_1(t)$ (black dashed curves) predicted by the probability of folded domains, $S_1(t) = \exp[-(1/r_f)\int_{0\to f} k_{\mathrm{unfld}}(f')\,\mathrm{d}f']$, and the correlations to unfolding rates at each ramp.

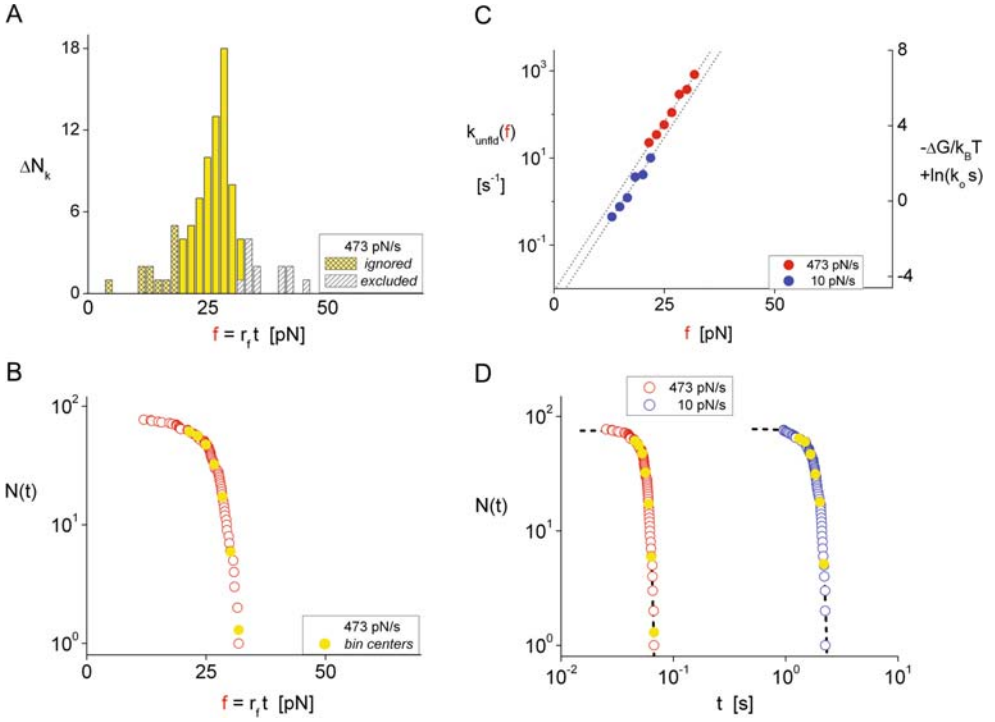

Figure 20.10. Rates of unfolding weak domains in poly-R16/I27 proteins under ramps of force. Used to assay the fastest unfolding rates at 473 pN/sec [3], the histogram of first unfolding events **(A)** provides the estimator for probability density; the corresponding array of statistics **(B)** provides the unnormalized estimator for the probability of remaining folded at different forces. [Again of no consequence in our analysis, we ignore the bins (marked by yellow meshes at low forces). The events in the cross-hatched bins (∼13% of total) have been truncated from the "raw statistics" to obtain the array $N(t)$. The Poisson fraction of putative multiples was determined from an attachment frequency of ∼26%.] Plotting the ratios of probability density/probability obtained at a fast and a slow [4] ramp on a logarithmic scale **(C)**, we see that the unfolding rates produced by the two ramps follow parallel lines (slope ∼2.8 pN) with a slight separation reflecting an approximate twofold difference in force-free unfolding rates (0.009/sec vs. 0.004/sec). **D.** Providing a critical check on quality of the assay for unfolding rates, experimental statistics for probabilities of remaining folded at the fast and slow ramps are compared on a log-log scale versus time to the unnormalized probabilities $N_0 S_1(t)$ (*black dashed curves*) predicted by the linear fits for unfolding rates (gray lines in panel C), that is, $N_0 \exp[-(1/r_f) \int_{0\to f} k_{\mathrm{unfld}}(f')\, \mathrm{d}f']$. The close match between the data and predictions reveals the major impact of ramp speed on unfolding kinetics.

20.7.2. Refolding Kinetics

Emphasizing the generality of our approach, we end by demonstrating that statistics of reverse transitions obtained with *negative* force ramps also provide a direct assay for refolding rates. Starting from an initial force f_0, each negative ramp applied to the unfolded chain in Figure 20.9 was produced by a fixed period of steady reduction in the trapping force at a rate $-r_f$, that is, $f(t) = f_0 - r_f\, t$. Accurately controlled in this way by laser power, the unloading process allowed the collapse and refolding of polyprotein domains previously unfolded by force. Usually, refolding is only likely to occur in a reasonable period of time when low levels of force are reached. Yet, at the same time, much larger forces are usually needed to initially unfold the domains. Thus, the sequence of positive– zero–*two* negative force ramps

was developed for the purpose of unfolding and refolding the R-16 domains, as illustrated in Figure 20.9.

In this example of refolding, we will use estimators for ratios of probability density/probability that characterize refolding from the level "2" to "1" identified by the labels above black dotted lines sketched in Figure 20.9. As seen throughout the slow negative ramp in Figure 20.9, transient up/down jumps appear along the length trace at all levels. Summarized by histograms in Figure 20.11A for unloading at –0.37 pN/s, the downward refolding events from a state of two to one unfolded domain ("2>1") appear as yellow bins, the intermittent-upward unfolding events returning to two unfolded domains ("2<1") as blue bins, and the downward refolding events from three to two unfolded domains ("3>2") as red bins. [The histrogram ("3<2") containing a few transient returns to the state of three unfolded domains is left out of Figure 20.11A for clarity.] Careful analysis (4) of the down/up jumps (e.g. "3<2" and "2<1") has revealed that refolding R-16 domains involves a long-lived metastable intermediate (mean lifetime ~0.3 s). Although complicated by the multi-level dynamics, we show that approximating the refolding process as a two-state transition provides a lower bound to the rates of refolding. As such, the statistical array N(f) for refolding from "2>1" plotted in Figure 20.11B becomes the un-normalized estimator for probability of two unfolded domains, which diminishes monotonically with increase in time or equivalently decrease in force. Using the arrays N(f) and histograms of transitions ("2>1") obtained with three negative ramps, we have plotted values (closed red, green, blue circles) of the approximation for ratios of probability density/probability on a logarithmic scale as a function of force squared (f^2/k_BT) and on a linear scale of rate versus force in Figure 20.11D. The estimates of refolding rates for the three negative ramps follow a negatively sloped line with a zero force intercept implying a spontaneous refolding rate of ~400/s from a state of two unfolded domains. Also plotted in Figure 20.11B is the un-normalized probability "N S2" derived from summation of all transitions to/from level "2" at –0.37 pN/s. Obtaining un-normalized probabilities in this way for each negative force ramp (details to appear elsewhere), and computing the true estimators for probability density/probability, the outcome (red dotted lines in Figures 20.11C, D) reveals that refolding actually occurs at much faster rates because of the transitions to/from the intervening metastable state. As indicated by the true estimators for probability density/probability (open red circles) from the fast unloading rate of –1.36 pN/s, the true refolding rates and the two-state approximation begin to converge when refolding rates greatly exceed the rate of transient unfolding from the metastable state. The reason for correlating the results to f^2/k_BT is that the unfolded domains are very floppy at low forces, and thus the energetics governing changes of end-to-end length is described by a harmonic potential [$\sim -f^2/(2\kappa_{chain})$]. Also following from polymer physics, the spring constant of the floppy chain κ_{chain} approximately equals the spring constant for a single unfolded domain κ_{unfld} divided by the number of unfolded domains, $\kappa_{chain} \approx \kappa_{unfld}/n_{unfld}$. Hence, the activation energy for refolding one domain is expected to be augmented by the difference in elastic energy required to shorten the chain, $\Delta[f^2/(2\kappa_{chain})]/\Delta n \approx f^2/(2\kappa_{unfld})$. Correlated to f^2/k_BT, the slopes obtained from linear regressions to the approximate and true refolding rates in Figure 20.11C yield apparent spring constants (0.22 and 0.28 pN/nm respectively) that characterize the apparent harmonic-energy barrier. These slopes bracket the harmonic stiffness, $3k_BT/(2bL_c) \approx 0.236$ pN/nm, based on persistence length ($b \sim 0.7$ nm) and contour length ($L_c \sim 37$ nm) used to match the force-distance response of the poly protein with all four R-16 domains unfolded. Converting the refolding kinetics in Figure 20.11C to a linear-linear scale, Figure 20.11D demonstrates the major suppression of refolding kinetics that accompanies pulling force.

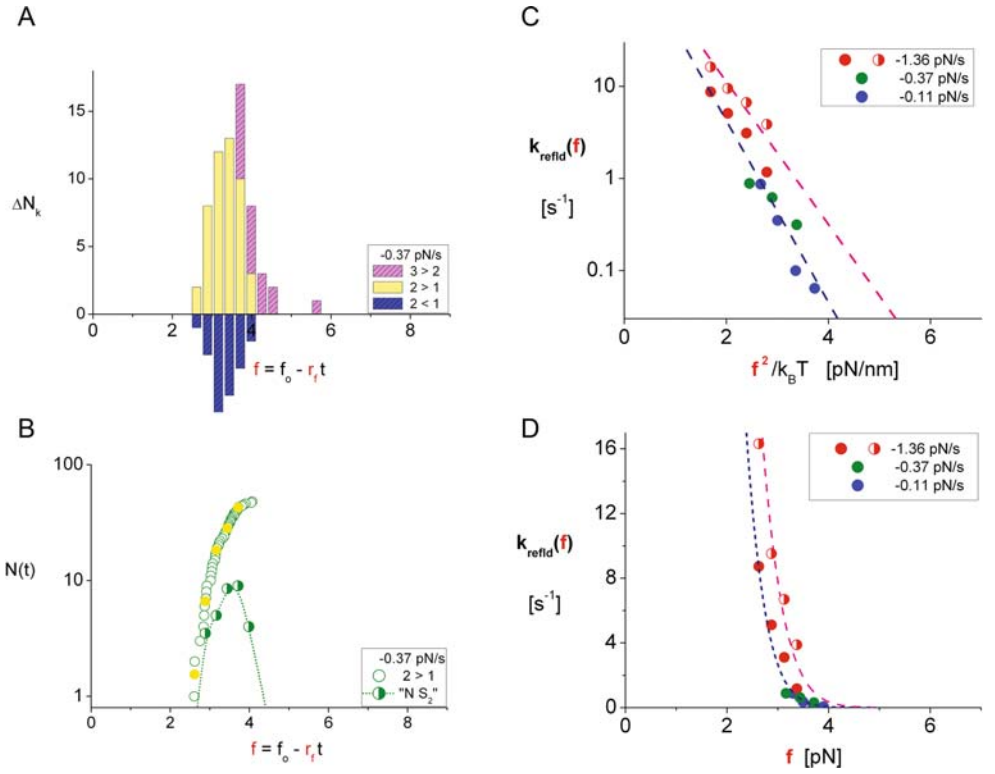

Figure 20.11. Rates of refolding (previously unfolded) domains in poly-R16/I27 proteins under *negative* ramps of force. Needed to assay the rates of refolding from level "2" to "1" in Fig. 9, histograms in **A** (plotted as forces) illustrate refolding and unfolding transitions that determine the un-normalized probability for being in a state with two unfolded and two folded domains under a negative ramp of –0.37 pN/s. Yellow bins show the downward refolding transitions to the state of one unfolded domain ("2>1"); blue bins show the intermittent-upward unfolding transitions returning to the state of two unfolded domains ("2<1"). Red bins show the downward refolding transitions to the state of two unfolded domains ("3>2") that seed level "2". [Not shown for clarity is the histrogram ("3<2") of transient returns to the state of three unfolded domains.] The statistical array N(f) of forces for refolding from "2>1" is plotted in **B** along with the un-normalized probability "N S_2" for being in level "2" computed from summation of all the transitions to/from this level. Naively approximating the refolding as a two-state process, the array N(f) plotted in **B** becomes the un-normalized estimator for probability of two unfolded domains, which diminishes monotonically with increase in time corresponding to the decrease in force. Using the arrays N(f) and histograms of transitions ("2>1") obtained with three negative ramps, we have plotted values (closed red, green, blue circles) for the approximate ratios of probability density/probability on a logarithmic scale as a function of force squared (f^2/k_BT) **(C)** and on a linear-linear scale versus force in **D**. The approximate refolding rates follow a negatively sloped line with a zero force intercept implying a spontaneous refolding rate of ~400/s given two unfolded domains. Also plotted for comparison, the outcome (red dotted lines) derived from the full multilevel analysis (details to appear elsewhere) shows that the two-state approximation provides a lower bound for the refolding rates at all forces. Illustrated by the true ratios of probability density/probability (open red circles) from the fast unloading rate of –1.36 pN/s, the true refolding rates approach the two-state approximation once refolding rates greatly exceed the rate of transient unfolding from an intervening metastable state.

Acknowledgment

This work was supported by National Institutes of Health grants HL65333 and HL31579.

References

1. Evans E, Ritchie K, Merkel R (1995) Sensitive force technique to probe molecular adhesion and structural linkages at biological interfaces. *Biophys. J*. 68: 2580–2587.
2. Evans E, Heinrich V, Leung A, Kinoshita K (2005) Nano-to-micro scale dynamics of P-selectin detachment from leukocyte interfaces: I. Membrane separation from the cytoskeleton. *Biophys. J*. 88: 2288–2298.
3. Halvorsen KA (2007) Probing weak single molecule interactions: development and demonstration of a new instrument. PhD dissertation, College of Engineering, Boston University, Boston MA.
4. Wong WP (2006) Exploring single-molecule interactions through 3D optical trapping and tracking: from thermal noise to protein refolding. PhD dissertation, Department of Physics, Harvard University, Cambridge MA.
5. Heinrich V, Wong WP, Halvorsen K, Evans E (2008) Imaging biomolecular interactions by fast three-dimensional tracking of laser-confined carrier particles. *Langmuir* 24: 1194–1203.
6. Williams P, Evans E (2002) In *Physics of Bio-Molecules and Cells*, *Les Houches: Ecoles d'Ete de Physique Theorique*, Vol. 75 (Springer, New York), pp. 186–203.
7. Lupher ML Jr, Harris EA, Beals CR, Sui L-M, Liddington RC, Staunton DE (2001) Cellular activation of leukocyte function-associated antigen-1 and its affinity are regulated at the I domain allosteric site. *J. Immunol*. 167: 1431–1439.
8. Beals CR, Edwards AC, Gottschalk RJ, Kuijpers TW, Staunton DE (2001) CD18 activation epitopes induced by leukocyte activation. *J. Immunol*. 167: 6113–6122.
9. Huth JR, Olejniczak ET, Mendoza R, Liang H, Harris EA, Lupher ML Jr., Wilson AE, Fesik SW, Staunton DE (2000) NMR and mutagenesis evidence for an I domain allosteric site that regulates lymphocyte function-associated antigen 1 ligand binding. *Proc. Natl. Acad. Sci. USA* 97: 5231–5236.
10. Evans E, Ritchie K (1997) Dynamic strength of molecular adhesion bonds. *Biophys. J*. 72: 1541–1555.
11. Evans E (2001) Probing the relation between force – lifetime – and chemistry in single molecular bonds. *Annu. Rev. Biophys. Biomol. Struct*. 30: 105–128.
12. Evans E, Williams P (2002) In *Physics of Bio-Molecules and Cells. Les Houches: Ecoles d'Ete de Physique Theorique*, Vol. 75 (Springer, New York), pp. 145–185.
13. Labadia ME, Jeanfavre DD, Caviness GO, Morelock MM (1998) Molecular regulation of the interaction between leukocyte function-associated antigen-1 and soluble ICAM-1 by divalent metal cations. *J. Immunol*. 161: 836–842.
14. Randles LG, Rounsevell RWS, Clarke J (2007) Spectrin domains lose cooperativity in forced unfolding. *Biophys. J*. 92: 571–577.
15. Forman JR, Clarke J (2007) Mechanical unfolding of proteins: insights into biology, structure and folding. *Curr. Opin. Struct. Biol*. 17: 58–66.
16. Scott KA, Batey S, Hootan KA, Clarke J (2004) The folding of spectrin domains I: Wild-type domains have the same stability but very different kinetic properties. *J. Mol. Biol*. 344: 195–205.